

The Mass distribution of the Cluster 0957+561 from Gravitational Lensing

Philippe Fischer ¹² and Gary Bernstein¹

Dept. of Astronomy, University of Michigan, Ann Arbor, MI 48109

George Rhee¹

Dept. of Physics, University of Nevada Las Vegas, Las Vegas, NV 89195

J. Anthony Tyson

Bell Laboratories, 600 Mountain Ave., Murray Hill, NJ 07974

ABSTRACT

Multiply gravitationally lensed objects with known time delays can lead to direct determinations of H_0 independent of the distance ladder if the mass distribution of the lens is known. Currently, the double QSO 0957+561 is the only lensed object with a precisely known time delay. The largest remaining source of systematic error in the H_0 determination results from uncertainty in the mass distribution of the lens which is comprised of a massive galaxy (G1) and the cluster in which it resides.

We have obtained V-band CCD images from CFHT in order to measure the mass distribution in the cluster from its gravitational distorting effect on the appearance of background galaxies. We used this data to construct a two-dimensional mass map of the field. A mass peak is detected at the 4.5σ level, offset from, but consistent with, the position of G1. Simple tests reveal no significant substructure and the mass distribution is consistent with a spherical cluster. The peak in the number density map of bright galaxies is offset from G1 similarly to the mass peak.

We constructed an azimuthally averaged mass profile centered on G1 out to $2'$ ($400h^{-1}$ kpc). It is consistent with an isothermal mass distribution with a small core ($r_c \approx 10'' = 33h^{-1}$ kpc). The inferred mass within 1 Mpc is consistent with the dynamical mass estimate but inconsistent with upper limits from a ROSAT X-ray study.

We discuss implications for H_0 in a future letter.

¹Visiting Astronomer, Canada France Hawaii Telescope

²Hubble Fellow

1. Introduction

One of the most interesting cosmological applications of gravitational lensing is the determination of Hubble's constant. This can be achieved by measuring the time delay between the observed light curves of multiply imaged QSOs (Refsdal, 1964). If the redshifts of the lens and source are known, and the mass distribution of the lens is well-understood, H_0 can be determined directly. Two advantages of this technique are that it is independent of the distance ladder-based methods and it is insensitive to motions of the nearby Universe.

The first-discovered doubly imaged quasar Q0957+561 (Walsh et al. 1979) has been the subject of intensive monitoring campaigns and is currently the only lensed system with a well-determined time delay (Thomson & Schild 1994, Schild & Thomson 1995, Turner 1996). The lens is comprised of a primary lens (the galaxy G1) and the cluster containing G1 (Young et al. 1981, Bernstein et al. 1993, Grogan & Narayan 1996). The largest remaining uncertainty in H_0 derived from this system is due to the uncertainty in the mass distribution in the lens, specifically, the ratio of the galaxy surface mass density to the cluster surface mass density.

An attempt has been made to measure the mass of G1 spectroscopically, yielding a velocity dispersion of $300 \pm 50 \text{ km s}^{-1}$ (Rhee 1991). However, this is a difficult measurement due to the proximity of the QSO B image. The spectroscopic value is somewhat lower than the $\sim 400 \text{ km s}^{-1}$ implied by the Faber-Jackson law (Bernstein et al. 1993).

In this paper we describe the direct measurement of the 0957+561 cluster surface mass density by studying its distorting effect on the appearance of background galaxies. This technique has recently been demonstrated to work well on massive clusters (e.g. Tyson et al. 1990, Tyson & Fischer 1995, Squires et al 1996), however, the cluster in the 0957+561 field is believed to be of significantly lower mass than previously studied clusters and will be a difficult test of the method.

In §2 and §3 we describe the observations and analysis. §4 describes the mass reconstruction techniques. §5 describes simulations which were carried out in order to calibrate the mass measurements and quantify the uncertainties and systematic errors in the analysis. §6 discusses the 2-d mass maps and azimuthally averaged radial mass profile, §7 compares the lensing results to previous mass determinations and §8 contains the conclusions and a description of some future work.

2. Observations

Twenty-nine 720s V-band images were taken of the region around the double quasar Q0957+561 using the Canada France Hawaii Telescope on 10-11 Jan 1994. FOCAM was used with the thick LORAL3 2048² CCD. This chip has 0.207" pixels and a field size 6' on a side. The effective field size is reduced somewhat because of vignetting at the corners due to the filter wheel. The conditions were photometric. The telescope was dithered between observations which allowed us to construct a flat-field from our observations. The final combined V-band image has a useable field size of 5.8' \times 5.5' with FWHM = 0.6" and the RMS noise of the sky is approximately 28.7 V mag per square arcsec (Fig. 1).

The photometric zeropoint for the 0957+561 V image was determined to an estimated accuracy of 0.03 mag from observations of five standard stars in the NGC 2264 field (Christian et al. 1985). Reddening in the 0957+561 field is low, E(B-V) < 0.03 mag (Burstein & Heiles 1982) so we assume E(B-V) = 0 in this paper.

We located 21 bright isolated stars with V < 23 to investigate the behaviour of the point-spread-function (PSF). These had measured ellipticities spanning $0.00 \leq \epsilon \leq 0.03$ ($\epsilon = 1-b/a$) with a mean of $\epsilon = 0.015$. The 20 objects with $\epsilon > 0$ have position angles ranging from $-55 < \text{PA (deg)} < 10$, implying a very slight position independent trailing, possibly arising from guiding errors or during the image combining procedure. This effect must be very small since any uncertainty in the ellipticity measurements of round objects will tend to result in an overestimate in the ellipticity on average. We test systematics arising from this PSF anisotropy by carrying out simulations using the PSF derived from the image (see §5).

3. Faint Galaxy Photometry and Analysis

The faint galaxy analysis was carried out using the analysis software ProFit (developed by PF). This software, starting with the brightest objects, fits an analytical model to each galaxy, using weighted, non-linear least squares, and subtracts the galaxy light from the image. It then proceeds to successively fainter objects. Once it has detected and subtracted all the objects in an image it replaces each galaxy in turn and refits and resubtracts until convergence is achieved. The software outputs brightness, orientation, ellipticity and other image parameters based on the fitted function. Fig 2 shows the final subtracted image.

Fig. 3 shows galaxy counts for the faint galaxies in the field of Q0957+561. The magnitudes are isophotal magnitudes with outer isophote of 27.8 mag square

arcsecond (31.2 mag per pixel). Also shown are recent V-band blank field counts from Smail et al. (1995); while the slopes of the counts are in good agreement, the Smail et al. counts lie about 45% below or 0.5 magnitudes to the right of our counts. Fig. 4 shows the size-magnitude relationship for the faint galaxies (r_h is the radius which contains half the light, uncorrected for seeing). The galaxy sequence is well-separated from the stellar sequence down to about 24th mag.

4. Mass Reconstruction

For gravitational lensing, the relationship between the tangential shear, γ_T , and surface mass density, Σ , is (Miralda-Escudé 1991, 1995),

$$\gamma_T(r) = \bar{\kappa}(\leq r) - \bar{\kappa}(r), \quad (1)$$

where $\kappa = \Sigma/\Sigma_{crit}$ and r is the radial distance from a given point in the mass distribution. The first term on the right is the mean density interior to r and the second term is the mean density at r . The basic technique for 2-d surface mass density reconstruction using the distortions of faint background galaxies is outlined in Kaiser & Squires (1993) (the KS algorithm). For a given coordinate on the image (\vec{R}), the distortion quantity for the i^{th} galaxy is:

$$D_i(\vec{R}) = \frac{1 - (b_i/a_i)^2}{1 + (b_i/a_i)^2} \times \frac{[\cos(2\theta_i)(\Delta x_i^2 - \Delta y_i^2) + 2 \sin(2\theta_i)\Delta x_i \Delta y_i]}{\Delta x_i^2 + \Delta y_i^2}, \quad (2)$$

where (b_i/a_i) and θ_i are the galaxy axis ratio and position angle, respectively. Δx and Δy are the angular horizontal and vertical distances from \vec{R} to galaxy i , and D is related to the tangential shear by $\gamma_T = (1 - \kappa) < D >$ for $\kappa < 1$. In the weak lensing regime $\kappa \ll 1$ and the surface mass density is given by:

$$\kappa(\vec{R}) = \frac{1}{\bar{n}\pi} \sum_{i=1}^N \frac{D_i(\vec{R})}{\Delta x_i^2 + \Delta y_i^2}, \quad (3)$$

where N is the number of galaxies and \bar{n} is the number density of galaxies. Eqn. 3 assumes that the galaxies are intrinsically (in the absence of lensing) randomly aligned. The critical density, Σ_{crit} depends on the redshift distribution of the background galaxies. Because of the random intrinsic alignments of the background galaxies, the formal error of κ from Eqn. 3 is infinite and in practice one must employ a smoothing kernel:

$$\kappa(\vec{R}) = \frac{1}{\bar{n}\pi} \sum_{i=1}^N \frac{W(\Delta x, \Delta y, s) D_i(\vec{R})}{\Delta x_i^2 + \Delta y_i^2} \quad (4)$$

In this paper we have used a smoothing kernel of the form (Seitz & Schneider 1995):

$$W(\Delta x, \Delta y, s) = 1 - \left(1 + \frac{\Delta x^2 + \Delta y^2}{2s^2}\right) e^{-(\Delta x^2 + \Delta y^2)/2s^2}, \quad (5)$$

where ‘ s ’ is referred to as the smoothing scale.

The 2-d mass map for the 0957+561 field is shown in Fig. 5. We discuss this further in §6.1.

Because of the smoothing kernel, plus biases introduced by edge effects in the images, this formula is mainly useful for determining the 2-d shapes of mass distributions. A less biased way of obtaining mass estimates as well as azimuthally averaged density profiles is (Fahlman et al. 1994):

$$\begin{aligned} \bar{\kappa}(r \leq r_i) - \bar{\kappa}(r_i \leq r \leq r_o) &= \frac{1}{\pi \bar{m}(1 - r_i^2/r_o^2)} \sum_{r_i \leq r \leq r_o} \frac{D_i(\vec{R})}{\Delta x_i^2 + \Delta y_i^2} \\ &= \frac{r_o^2}{M} \sum_{r_i \leq r \leq r_o} \frac{D_i(\vec{R})}{\Delta x_i^2 + \Delta y_i^2}, \end{aligned} \quad (6)$$

where M is the number of galaxies between r_i and r_o , and \bar{m} is the corresponding number density.

In the upper panel of Fig. 6 we show the calibrated 0957+561 cluster radial mass density profile resulting from Eqn. 6. The error bars are based on the 1σ galaxy-to-galaxy scatter of the values inside the sum in Eqn. 6. A discussion of Calibration and systematic errors and an interpretation of the radial mass profile can be found §5.

It should be mentioned that galaxy distortion is insensitive to flat sheets of mass. Consequently, all mass measurements described in this paper are uncertain by an unknown additive constant. If there is a substantial flat component to the mass distribution our mass estimates will be lower limits (see §6.2).

5. Calibration and Systematics

Application of the mass reconstruction techniques described above will result in underestimates of the mass due to: measurement error, the effects of seeing, and the intrinsic ellipticity of the background galaxies. These effects must be calibrated in order to correct the mass estimates. Calibration was carried out using two methods. The first was a full Monte-Carlo simulation of the data and

the second involved applying a known constant shear to the Hubble Deep Field (HDF) (Williams et al. 1995).

5.1. Monte-Carlo Simulations

Aside from calibrating the lensing results, simulations of the observational data are useful for quantifying systematics in the inferred mass distributions.

The simulations consisted of artificial galaxies distributed in seven redshift shells ($z = 0.0 - 0.355, 0.355 - 0.5, 0.5 - 0.65, 0.65 - 0.8, 0.8 - 1., 1.0 - 2.0, 2.0 - 7.2$). For each shell, simulated images were made with pixels equal to one quarter the area of the pixels on the observed image. Galaxy images were generated for each shell based on the quiescent models of McLeod & Rieke (1995). Briefly, the McLeod & Rieke models involve six galaxy types (E, S0, Sab, Sc, Sd, Im) with a formation epoch of $z = 7.2$. $H_0 = 60 \text{ km s}^{-1} \text{ Mpc}^{-1}$ and $q_0 = 0.05$ were assumed. Evolution and k-corrections are based on the synthesis models of Bruzual & Charlot (1993). Bulge-to-disk ratios were taken from King & Ellis (1985). The model counts were normalized to fit our V-band galaxy counts. Stars were also added to the simulated images based on the observed star counts (measured for $V < 24$ and extrapolated with the same slope to the detection limit).

Initially we used galaxy size - absolute magnitude relationships from Im et al. (1995), however, these were seen to produce apparent magnitude - size relationships substantially larger than observed for $V > 24$. Smail et al. (1995) also saw small galaxy sizes for $V > 24$ with similar image quality. The evolution of galaxy sizes (as well as other aspects of galaxy evolution) is not well understood. One explanation for the small galaxies we observe is that we are seeing more small galaxies at low to intermediate redshift than predicted by the McLeod & Rieke models. This might also explain why these models underpredict the density of apparently faint galaxies. Alternatively, higher redshift galaxies may have their emission more concentrated towards their centers than local galaxies or we may be seeing small emitting regions within the galaxies. It is not currently possible to distinguish between these (and other) scenarios so for the present work, we arbitrarily assume that the galaxy sizes evolve as $(1+z)^{-1}$, which was seen to provide good agreement with the faint galaxy measurements down to the detection limit (see Fig. 4).

The galaxies in each shell were distorted with various spherically symmetric mass distributions located at $z=0.355$ under the assumption that all galaxies within a shell lie at the number weighted mean redshift of that shell. The distorted images were combined and convolved with the slightly elongated PSF

derived from the observations. The images were block-summed 2×2 and Gaussian noise was added. The simulated images were processed identically to the observed images.

Fig. 3 shows the observed galaxy counts of one of the simulated data frames superimposed on the 0957+561 galaxy counts. Assuming the input galaxy counts are correct, the completeness curves are in excellent agreement, giving us confidence that the size-magnitude relationship is correct. Fig. 7 shows ellipticity histograms for data and one of the simulations. These look similar, although the simulation has a mean ellipticity of around 0.24 versus 0.27 for the data. It is important that the simulated and real galaxies are well matched in both ellipticity and size since the response of a galaxy under shear (the “shear polarizability” - see Kaiser et al. 1995) is dependent on these two parameters.

5.2. Hubble Deep Field Simulations

Compared to the CFHT data the HDF data is both much higher resolution and much deeper. Therefore, it offers an excellent opportunity to calibrate our mass estimates as described in Kaiser et al. (1995). The technique involves stretching the HDF data by $1 + \delta$, convolving with the PSF and adding noise. The values of D_i are measured for each galaxy and compared to the unstretched values of D_i . The quantity of interest is the recovery factor, $C = \delta / \langle \Delta D_i \rangle$. The raw values of κ are then multiplied by $\langle C \rangle$ to yield the corrected values. One problem is that the HDF V-band filter (F606W) is significantly different from our V-band filter in both central wavelength and width. In order to insure that we were sampling the same population of galaxies we chose a 2.5 magnitude range in the HDF data which yielded the same surface number density of galaxies as in our field for the range $24.0 \leq V \leq 26.5$ (see §6.1). This turned out to be $23.5 \leq F606W_{HDF} \leq 26.0$. We stretched the HDF data in four different directions with $\delta = 0.053$ (the mean value of the shear due to the cluster) and obtained a value of $\langle C \rangle = 2.4 \pm 0.2$.

Unfortunately, this value cannot be compared directly to the value obtained from the Monte-Carlo simulations since the latter is dependent on the redshift distribution of the background galaxies. Since the galaxies we used ($24.0 \leq V \leq 26.5$) have little or no redshift information available we must rely on the model described above to extrapolate the known redshift distribution. This is complicated somewhat by the fact that our detection completeness starts to fall below 100% for galaxies with $V > 25.5$. Our best estimate for the mean redshifts of our background galaxies is $\langle z_b \rangle = 1.2$, implying $\Sigma_{crit} = 4200 - 4700h^{-1}M_\odot$

pc⁻² for $\Omega = 0 - 1$. The value of Σ_{crit} varies by $\pm 10\%$ for $< z_b > = 0.95$ and 1.7. Moving the mean redshift to $z_b = 3$ decreases Σ_{crit} by 17%.

The recovery factor from the Monte-Carlo simulations is

$$C = 2.3 \pm 0.05 \frac{\Sigma_{crit}(< z_b >) }{\Sigma_{crit}(< z = 1.2 >)}, \quad (7)$$

smaller but easily consistent with the value from the stretched HDF images.

6. Discussion

6.1. 2-d Mass Maps

The 2-d, KS mass map for our data is shown in Fig. 5 superposed on the V-band image of the field. This reconstruction used 1651 galaxies with $24.0 \leq V \leq 26.5$. The detection of the central peak is significant at around the 4.5σ level based on the scatter in the simulations.

The first thing the simulations can reveal are systematic errors in the 2-d mass map due to the elongated PSF and the finite size of the image. In Fig. 8 we show the average mass map from 153 Monte Carlo simulations of a spherical cluster which fits our data well (§6.2). There is some evidence for small spurious features: a slight elongation in the north-south direction and 1σ negative features along all four edges. These systematics are what is expected from the KS algorithm (Schneider 1995), and become more serious as the distance from the image center increases. Therefore, in order to quantify measurements made with the mass map we will use the simulations as a comparison.

The isodensity contours in Fig. 5 are not identical to the mean of the simulations. Is this a significant departure from circular symmetry or just the noise in the KS reconstruction? The issue of substructure is an important one from the perspective of H_0 determination. There is spectroscopic evidence for the existence of a poor cluster at $z=0.5$ (Garrett et al. 1992, Angonin-Willaime et al. 1994) centered about 81'' west and 43'' north of G1. As pointed out in Bernstein et al. (1993), if sufficiently massive, this cluster may be an important constituent of the lens.

In order to test the significance of the deviations from circularity in the KS mass reconstruction (Fig. 5), we compute its ellipticity from the quadrupole moments of the portions of the map with $\kappa > 0$. Fig. 9 shows this ellipticity value along with the distribution of ellipticities measured in an identical manner from the Monte-Carlo simulations, which all contain perfectly circular mass distributions. The 0957+561 map is a bit rounder than the mean of the simulations but

well within the normal range. Therefore we conclude that we have not detected substructure in our cluster. It should be noted that we have used a smoothing scale of $s = 30''$ and substructure finer than this would be washed out. Probing higher resolution substructure needs a higher density of background galaxies, requiring deeper images with better seeing.

Also of interest for H_0 determination is the accuracy of the mass centroid measurement. The mean of the centers of the 153 simulations show no systematic deviations from the input center. The 1σ uncertainty in the position of the centers is $15''$. From Fig. 5, the center of mass in the 0957+561 field is located $\sim 22''$ from the galaxy G1 ($18''$ east $13''$ north of G1). zconsistent with the position of G1 at the 1.5σ level. The direction of the offset appears to be consistent with that found by Dahle et al. (1994) using 123 galaxies (compared to 1651 in this study) although our offset is larger. These two measurements are not completely independent since many of the arclets near the QSO will be common to both studies. Fig. 10 is a contour plot of galaxy number density for $V < 24$. There is a 3σ peak offset from G1 in the same direction as the mass peak lending support to the idea that G1 is not at the center of mass. In order to avoid biasing our result, we have adopted G1 as the mass center for our azimuthally averaged mass density profile described below.

6.2. Mass Profile

The azimuthally averaged mass density profile centered on the galaxy G1 as derived from the weak lensing approximation (Eqn. 6) is shown in the upper panel of Fig. 6. The individual points shown in this plot are not independent since values at large radii contain a subset of the galaxies used to determine quantities at smaller radii.

Comparing our surface density profile to a variety of spherical cluster simulations with isothermal plus core profiles we find good agreement between data and simulations for:

$$\Sigma(r) = \Sigma_0 [1 + (r/r_c)^2]^{-1/2}, \quad (8)$$

with $r_c = 10''$ and $\Sigma_0 = 2600 \pm 800h M_\odot \text{ pc}^{-2}$. There is some marginal evidence that the mass profile falls off faster than isothermal for $r > 400 \text{ kpc } h^{-1}$ however the uncertainties are large at these radii and a bigger field is required to test this hypothesis.

As can be seen in the upper panel of Fig. 6 the mean surface mass density of the simulated clusters determined under the weak lensing approximation deviates

substantially from the input surface mass density. To explore this further, Fig. 11 shows a plot of the mean of simulations for two different spherical isothermal plus core mass distributions (with similar total mass to the 0957+561 cluster). Both models show a tendency for the derived profiles to be steeper than the input models. We attribute this effect to the breakdown of the weak lensing approximation. Because we know the true density profile for these simulations we can test this hypothesis by removing the weak lensing assumption and seeing if the agreement improves. This amounts to modifying Eqn. 6 to the following form:

$$\bar{\kappa}(r \leq r_i) - \bar{\kappa}(r_i \leq r \leq r_o) = \frac{r_o^2}{M} \sum_{r_i \leq r \leq r_o} \frac{D_i(\vec{R})[1 - \kappa(\vec{R})]}{\Delta x_i^2 + \Delta y_i^2} \quad (9)$$

The value of $\kappa(\vec{R})$ for each galaxy assumes Σ_{crit} appropriate to the *mean* redshift of the background galaxy sample of $z = 1.2$ (§5.2). Fig. 11 shows the results of the modified mass inversion. The agreement between the input and inferred mass density is much improved with no sign of systematic deviations. Therefore, for subcritical lenses, one can hope to recover information in the intermediate-lensing regime either by fitting the data directly to the results of the simulations (which should suffer from the same systematics) or, non-parametrically, by adopting an iterative approach where the first step assumes the weak lensing approximation and subsequent steps use the previous value of the (smoothed) density profile to estimate the $(1 - \kappa)$ term in Eqn. 9. We have adopted the former technique and show the profile corrected for $(1 - \kappa)$ (from the best-fit simulated data) in the lower panel of Fig. 6.

It is possible that the simulated data corrects better than real data because of the finite width of the redshifts shells. However, in our simulations, there are shells with significant numbers of detected galaxies which have mean redshifts both higher and lower than the mean redshift of the whole sample, so we feel this is a fair representation of the real data.

Fig. 12 shows a plot of calibrated $\langle D_i(r) \rangle = \gamma_T(r)/[1 - \kappa(r)]$ in radial bins around G1. These points, though noisy, are independent. The reduced χ^2 between the points and model line in Fig. 12 is 0.62, however, due to the large error bars on the points it is not possible to provide strong constraints on the shape of the profile. The value of $\langle \gamma_T(r)/[1 - \kappa(r)] \rangle$ for the entire radial range $10'' \leq r \leq 168''$ is 0.053 ± 0.016 ($s/n = 3.4$).

The Monte-Carlo simulations provide a good check on our error analysis. In Fig. 6 we show the surface density and uncertainty derived from the data along with the mean and scatter of the simulations. The two sets of error estimates

are in excellent agreement. The s/n of the density estimates decreases at the smallest radii due to sensitivity to the presence of a small number of radially or tangentially aligned galaxies. This results because of $\frac{1}{\Delta x^2 + \Delta y^2}$ in the denominator of Eqn. 6. For example, by removing the four most extreme galaxies, the apparent s/n increases from around 3 to 4.

As mentioned, the best fit model to the data has $r_c = 10'' = 33h^{-1}$ kpc. However, this is quite dependent on the innermost point in Fig. 6 which, as just described, is very sensitive to a small number of galaxies. Therefore, it is possible that the core radius could be substantially in error. At the low end, it is impossible to rule out $r_c = 0$. At the high end, lowering the innermost point 1σ yields $r_c = 15'' = 50h^{-1}$ kpc.

One systematic that we do not account for in our Monte-Carlo simulations is contamination of our field galaxy sample by cluster galaxies. If cluster galaxies have been included in our mass reconstruction then we will have underestimated the mass density. If the cluster galaxies are concentrated towards the center of the cluster (as one would expect) then we would also be underestimating the steepness of the mass profile. Because of the difficulty in distinguishing possible cluster galaxies from the field galaxy population we have not attempted to correct for contamination. However, a surface number density map of all galaxies used in the mass reconstruction ($24 < V < 26.5$) reveals no significant concentrations centered near G1 (or any significant density fluctuations in the field), so we conclude that any cluster galaxy contamination is small.

The surface mass density estimates discussed in this section are determined from measurements of density *contrasts* between inner regions and control annuli (Eqn. 6). Therefore an estimate of the *total* surface density requires that we estimate the mass densities of the control annuli. This was implicit in our assumption of the functional form in Eqn 8 for the cluster mass distribution. Because this estimate is based on an extrapolation of our measurements to a region which we cannot measure, it is worth mentioning the size of the correction. For the innermost point ($r = 10''$), the mean density of the control annulus is around 13% of the interior mean density. This rises to about 25% for our outermost point. There is some marginal indication from the density profile that the mass density falls off more sharply than our model. If this is true then the mass densities of the control annuli are overestimated and the mass densities in this paper will be overestimated. Alternatively, if the mass densities in the control annuli are underestimated (perhaps there is a flat component to the cluster mass density), then the mass densities are underestimated.

7. Other Mass Determinations

Previous attempts to measure the cluster mass in the 0957+561 field include a radial velocity study and an X-ray study.

Garrett et al (1992) and Angonin-Willaime et al. (1994) measured redshifts for 21 probable cluster members, obtaining a velocity dispersion of $\sigma = 715 \pm 130$ km s $^{-1}$. If one assumes a singular isothermal mass distribution and an isotropic phase space distribution function, the implied mass contained within a projected radius of 1 Mpc is $M(r < 1 \text{ Mpc}) = 3.7_{-1.2}^{+1.5} \times 10^{14} \text{ M}_\odot$. Of course uncertainties in the distribution function and problems with field galaxy contamination imply a much higher uncertainty. In any case, extrapolating our model with $\Sigma_0 = 2600 \pm 800h \text{ M}_\odot \text{ pc}^{-2}$ and $r_c = 33h^{-1} \text{ kpc}$ implies a mass of $M(r < 1 \text{ Mpc}) = 5.3 \pm 1.6 \times 10^{14} \text{ M}_\odot$, consistent with the dynamical mass estimate.

Based on ROSAT PSPC and HRI data of the 0957+561 field, Chartas et al. (1995) place upper limits on the cluster temperature and mass. They obtained a 3σ upper limit on the cluster mass within a projected radius of 1 Mpc of G1 of $1.5 \times 10^{14} \text{ M}_\odot$, significantly lower than the lensing mass estimate.

8. Conclusion

The double QSO Q0957+561 was the first multiply gravitationally lensed system discovered (Walsh et al. 1979). It is currently the only lensed system with a firm time-delay. Extensive modeling has been carried out for this system and the conclusion is that in order to constrain H_0 the mass distribution in the lens must be better understood (Grogin & Narayan 1996 and references therein). The lens consists of the galaxy G1 and the cluster to which G1 belongs.

In this paper we have determined the mass distribution in the $z=0.355$ cluster in the field 0957+561 by studying the distorted appearance of faint background galaxies with $24.0 \leq V \leq 26.5$. We derived the 2-d mass distribution which appears to be consistent with a spherical cluster given our smoothing scale of $s = 30''$. The mass centroid is located $22''$ from the dominant cluster galaxy G1, but is consistent with the galaxy position at the 1.5σ level. A density map of galaxies with $V < 24.0$ has a peak, offset from G1 in the same direction as the mass map strengthening the argument that G1 is offset from the center of mass.

We have calculated the azimuthally averaged mass profile centered on G1 out to $400h^{-1} \text{ kpc}$. It is well fit by an isothermal model possessing a core of $r_c = 10'' = 33h^{-1} \text{ kpc}$.

In terms of total mass, good agreement is seen with previous kinematic measurements under the assumption of isotropy. Our gravitational lensing mass,

however, disagrees with upper limits based on X-ray data.

We will discuss the implications for H_0 in a companion paper.

Support for this work was provided by NASA through grant # HF-01069.01-94A from the Space Telescope Science Institute, which is operated by the Association of Universities for Research in Astronomy Inc., under NASA contract NAS5-26555. George Rhee acknowledges travel support from the UNLV Physics department Bigelow fund. Thanks to: Ian Smail for providing his V-band galaxy counts and Brian McLeod for assistance in reproducing his galaxy evolution models.

REFERENCES

Angonin-Willaime, M.-C., Soucail, G. & Vandervriest, C. 1994, *A&A*, 291, 411.

Bernstein, G. M., Tyson, J. A., & Kochanek, C. S. 1993, *AJ*, 105, 816.

Bruzual, A. G., & Charlot, S. 1993, *ApJ*, 405, 538.

Burstein, D. & Heiles, C. 1982, *AJ*, 87, 1165.

Chartas, G., Falco, E. Forman, W., Jones, C. Schild, R. & Shapiro, I., *ApJ*, 445, 140.

Christian, C. A. et al. 1985, *PASP* 97 363.

Dahle, H., Maddox, S. J., & Lilje, P. B. 1994, *ApJL*, L79.

Fahlman, G.G., Kaiser, N., Squires, G. & Woods, D. 1994, *ApJ*, 436, 56.

Garrett, M. A., Walsh, D. & Carswell, R. F. 1992, *MNRAS*, 254, 27p.

Grogin, N. A. & Narayan, R. 1996, *ApJ*, 464, 92.

Im, M., Casertano, S. Griffiths, R. E., Ratnatunga, K. U. & Tyson, J. A. 1995, *ApJ*, 441 494.

Kaiser, N. & Squires, G. 1993, *ApJ*, 404, 441

Kaiser, N., Squires, G. & Broadhurst, T. 1995, *ApJ*, 449, 460.

King, C. & Ellis, R. 1985, *ApJ*, 288, 456.

McLeod, B. A., Rieke, M. J. 1995, *ApJ*, 454, 611.

Miralda-Escudé, J. 1991, *ApJ*, 370, 1.

Miralda-Escudé, J. 1995, in “IAU 173: Astrophysical Applications of Gravitational Lensing”, eds. C. S. Kochanek & J. N. Hewitt, (Kluwer), p. 131.

Refsdal, S. 1964, MNRAS, 128, 307

Rhee, G. 1991, Nature, 350, 211

Schneider, P. 1995, A&A, 302, 639.

Schild, R, & Thomson, D. J. 1995, AJ, 109, 1970.

Seitz, C. & Schneider, P. 1995, A&A, 297, 287.

Smail, I, Hogg, D. W., Yan, L. & Cohen, G. 1995, ApJL, L105.

Squires, G, et al 1996, ApJ, 461, 572.

Thomson, D. J., & Schild, R, 1994, in Proceedings of the International Conference on Applications of Time Series Analysis in Astronomy and Meteorology (in press).

Turner, E. 1996, private communication.

Tyson, J. A. & Fischer, P. 1995, ApJL, L55.

Tyson, J.A., Valdes, F. & Wenk, R.A. 1990, ApJ, 349, L1.

Walsh, D., Carswell, R. F., Weymann, R. J., Nature, 279, 381.

Williams, R. E. et al. 1995, BAAS, 187.0903.

Young, P., Gunn, J. E., Kristian, J., Oke, J. B., & Westphal, J. 1981, ApJ, 244, 736.

Fig. 1.— V-band CFHT image of the field centered at 0957+561. The image is $5.8' \times 5.5'$, north is at the top and east is to the left. The total exposure time is 5.8 hours. The seeing is FWHM = $0.6''$ and the RMS noise of the sky is approximately 28.7 V mag per square arcsec. The image intensity scaling is logarithmic.

Fig. 2.— The same as Fig. 1 after ProFit galaxy fitting and subtraction.

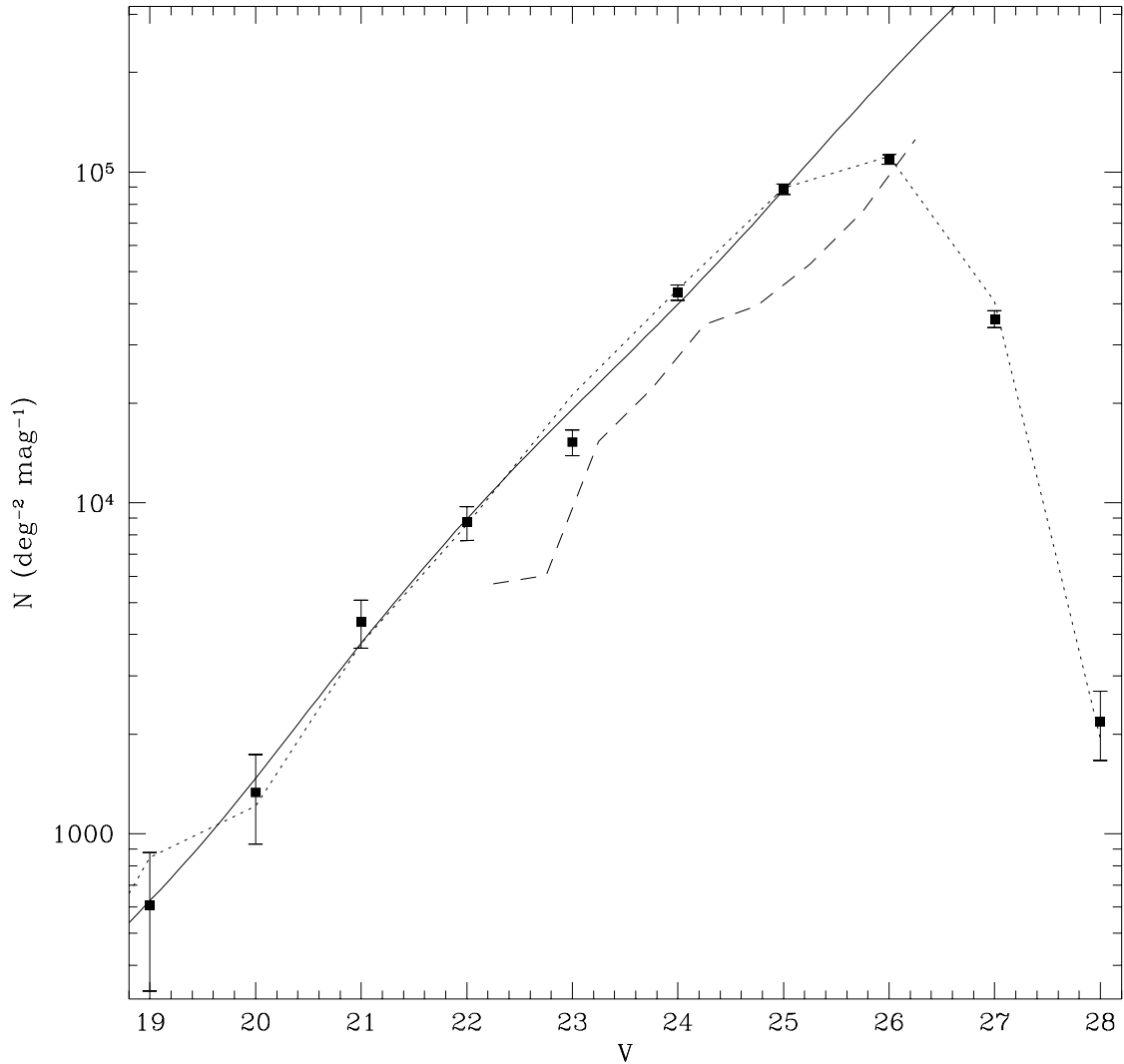


Fig. 3.— Galaxy plus star counts for the observed image (points) and one of the simulations (dotted line). The galaxy magnitudes are isophotal magnitudes with outer isophote of 27.8 mag square arcsecond. The error bars are based on Poisson statistics. The solid line shows the input function for stars and galaxies. Also shown are recent V-band counts (dashed line) from Smail et al. (1995) which are about 45% below or half a magnitude to right of the 0957+561 counts.

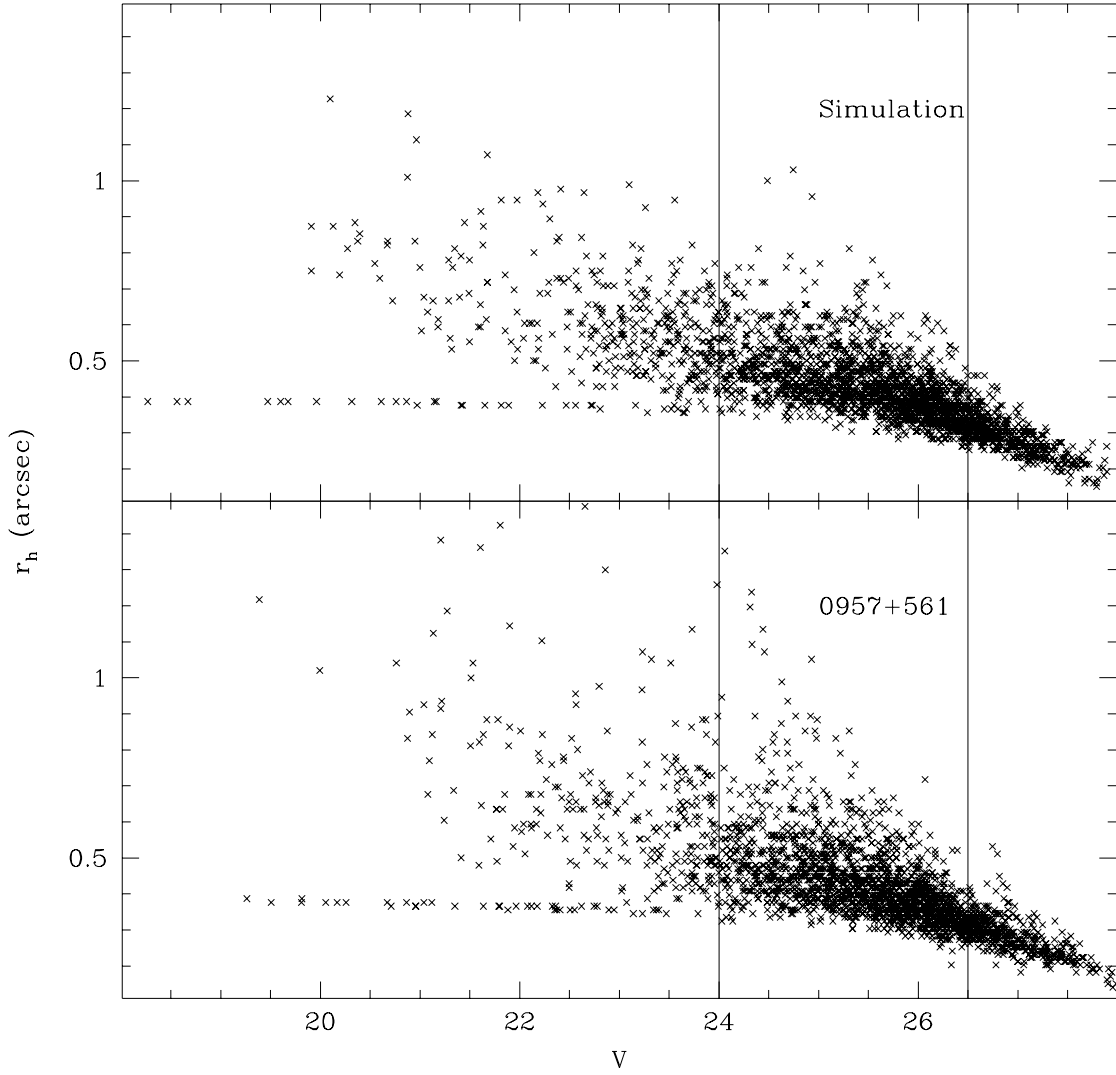


Fig. 4.— Half light radius vs. apparent V magnitude for the data (lower panel) and one of the Monte-Carlo simulations (upper panel). The radii are not corrected for seeing. Good quantitative agreement is seen. The vertical lines indicate the magnitude range of galaxies used in the mass reconstruction

Fig. 5.— Mass map of the 0957+561 field using the technique of Kaiser & Squires (1993) superimposed on a V-band CCD image. A total of 1651 galaxies (arclets) with $24.0 \leq V \leq 26.5$ were used in the reconstruction and the the smoothing scale is $s = 30''$. The contours are stepped in units of 0.5σ . North is up and East is to the left. The displayed field is $327''$ on a side.

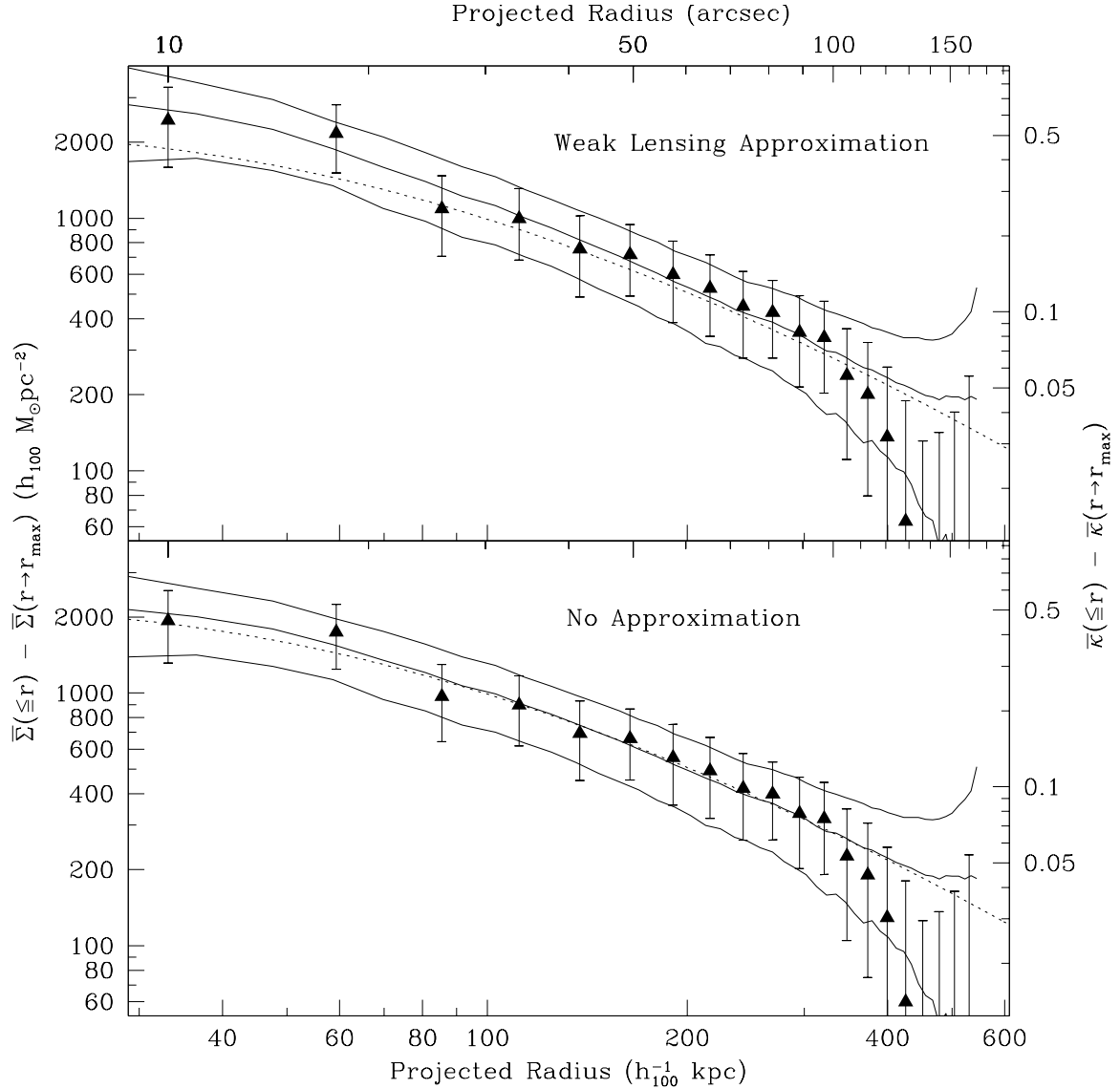


Fig. 6.— The upper panel is the radial mass density profile for the 0957+561 cluster from Eqn. 6 (weak lensing approximation) centered on G1. The points are the data for the cluster derived from 1307 galaxies having $24.0 \leq V \leq 26.5$. The solid line is the mean profile and the 1σ upper and lower limits for 153 simulations of a spherical cluster having $r_c = 10'' = 33h^{-1}$ kpc and $\Sigma_0 = 2600hM_\odot \text{ pc}^{-2}$. $r_{max} = 168'' = 550h^{-1}$ kpc. The input model is shown by the dotted line. The lower panel is the radial density profile from Eqn. 9. Both the data and the simulations have been corrected by $(1 - \kappa)$ using the input profile for the simulations which is a power-law plus a core as described in the text (see §6.2).

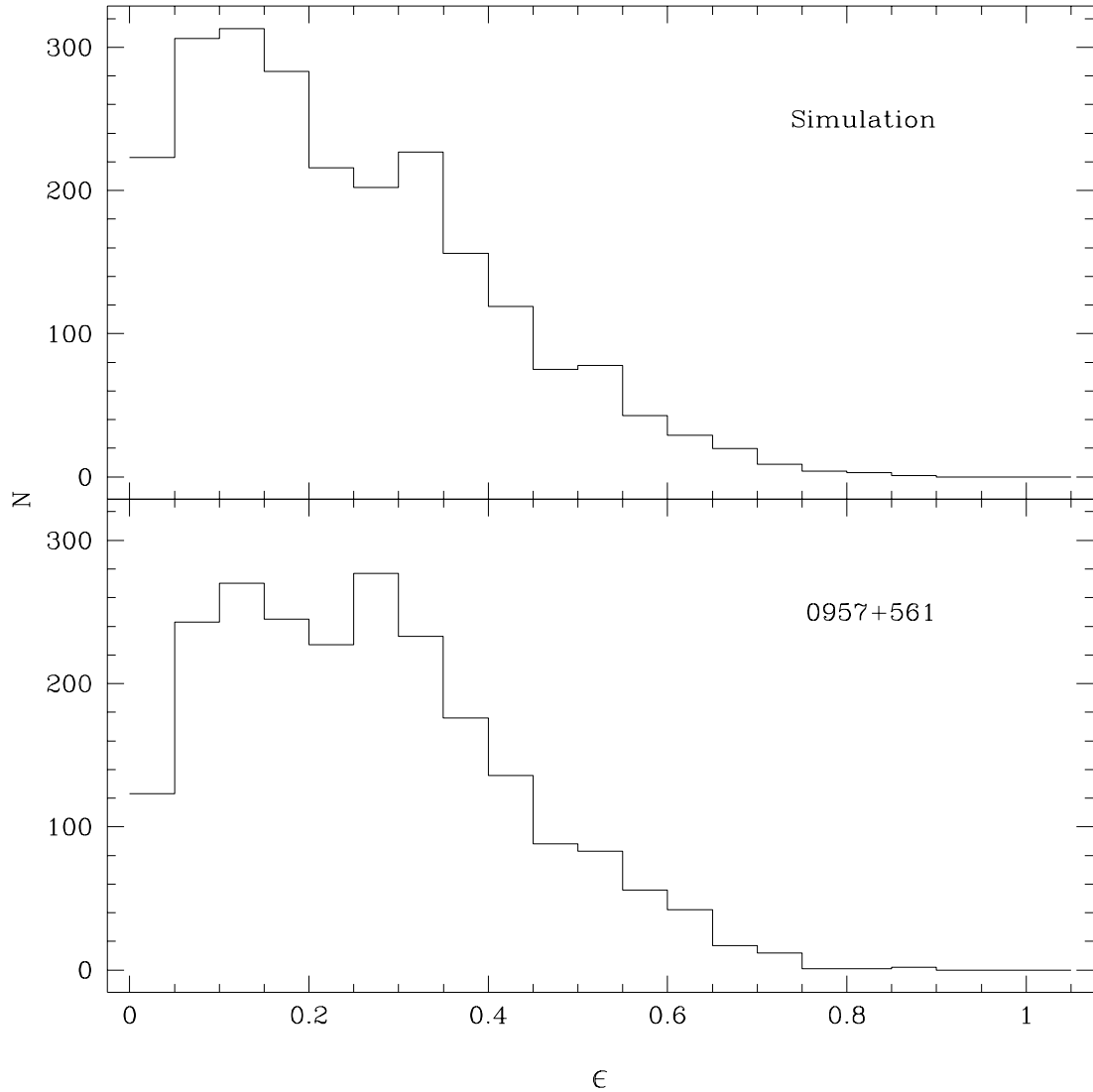


Fig. 7.— Ellipticity histograms for galaxies in the 0957+561 field and one of the simulations. The shapes are similar, however, the mean ellipticity of the simulation is 0.24 versus 0.27 for the data.

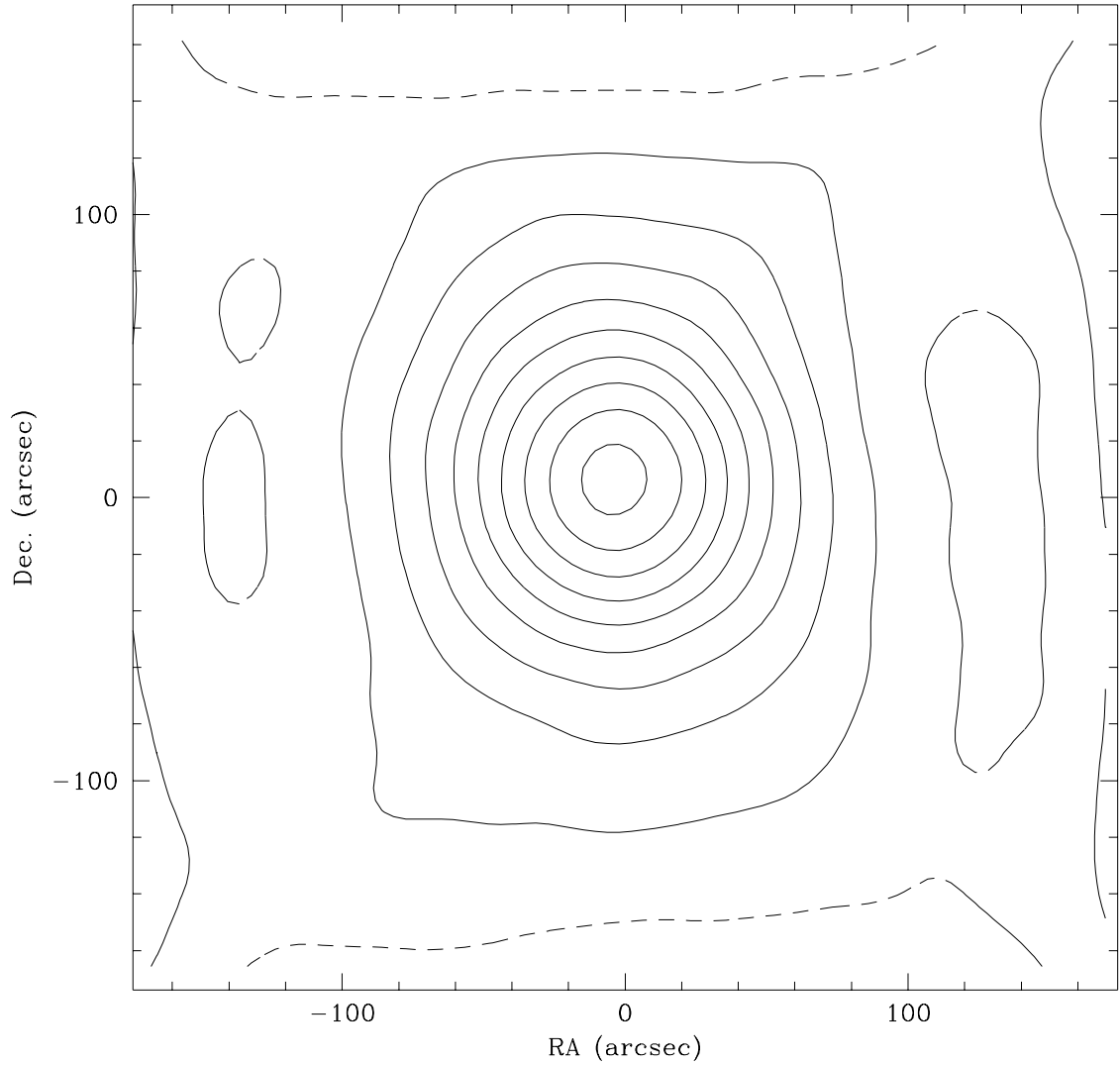


Fig. 8.— Mean mass map for 153 simulations of a spherical cluster. The smoothing scale is $s = 30''$. The contours have steps of approximately 0.5σ of an individual image. Edge effects are apparent as well as a small vertical elongation.

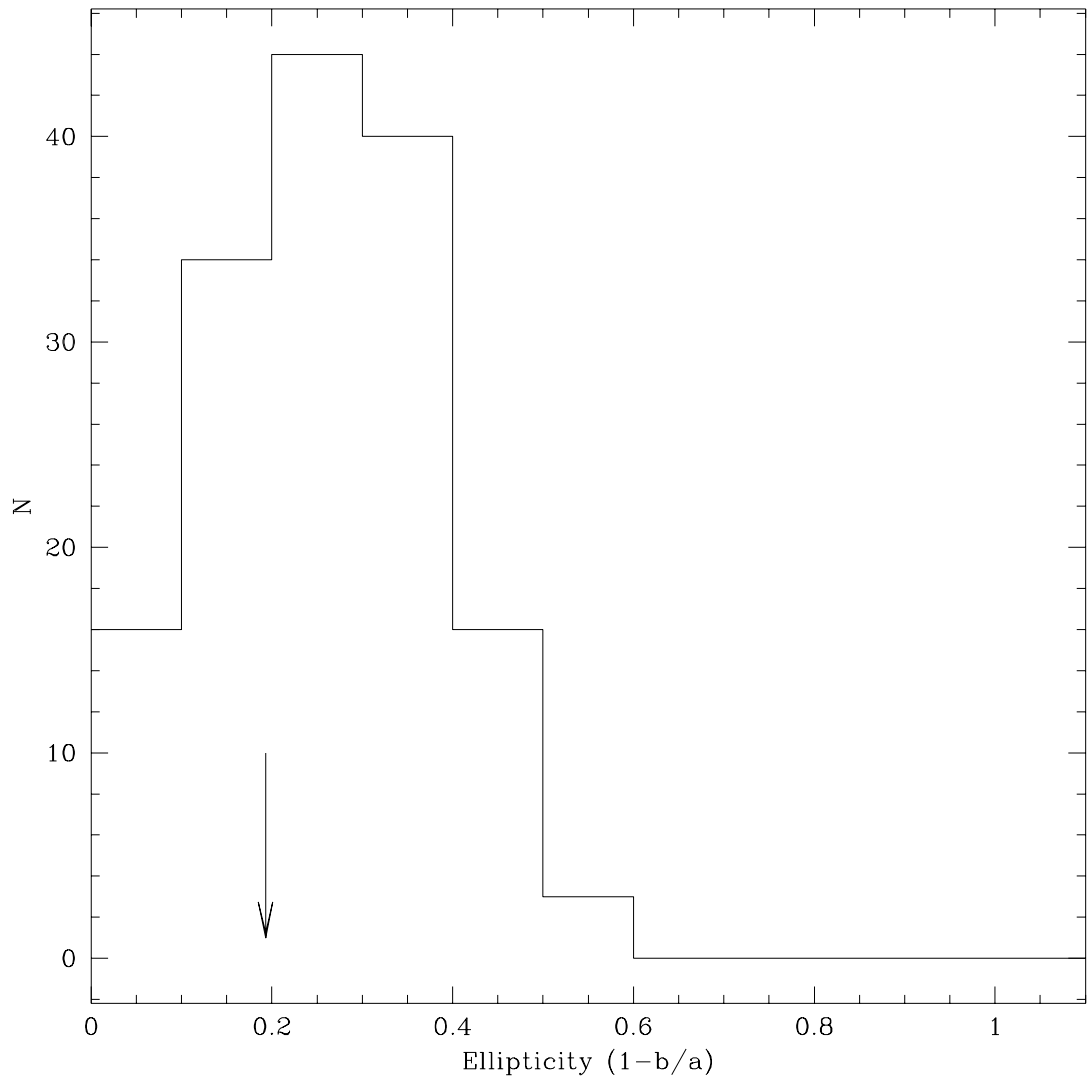


Fig. 9.— Ellipticity histograms of the simulated mass maps. The input models have $\epsilon = 0$. The arrow indicates the measured value for the 0957+561 field.

Fig. 10.— Contours of galaxy surface number density for $V < 24$ in steps of 0.5σ about the mean. A total of 302 galaxies were used and a Gaussian smoothing with $\sigma = 30''$ has been applied.

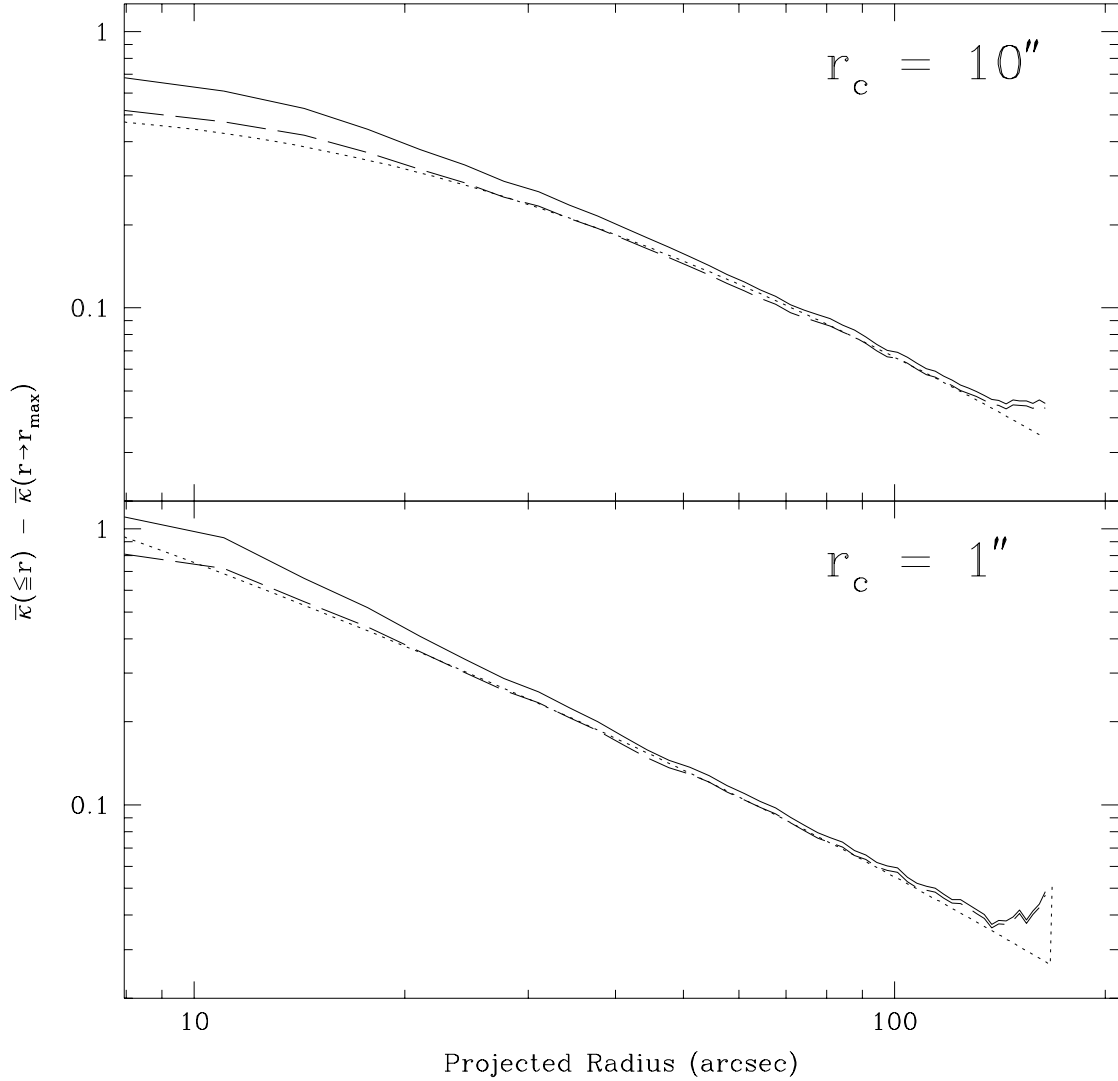


Fig. 11.— Input and calibrated output radial profiles for two sets of simulations of isothermal lenses. The lower panel (100 simulations) has $r_c = 1''$ and the upper panel (153 simulations) has $r_c = 10''$. The input models are the dotted lines. The solid lines are the output profiles under the weak lensing approximation while for the dashed lines no approximation has been made.

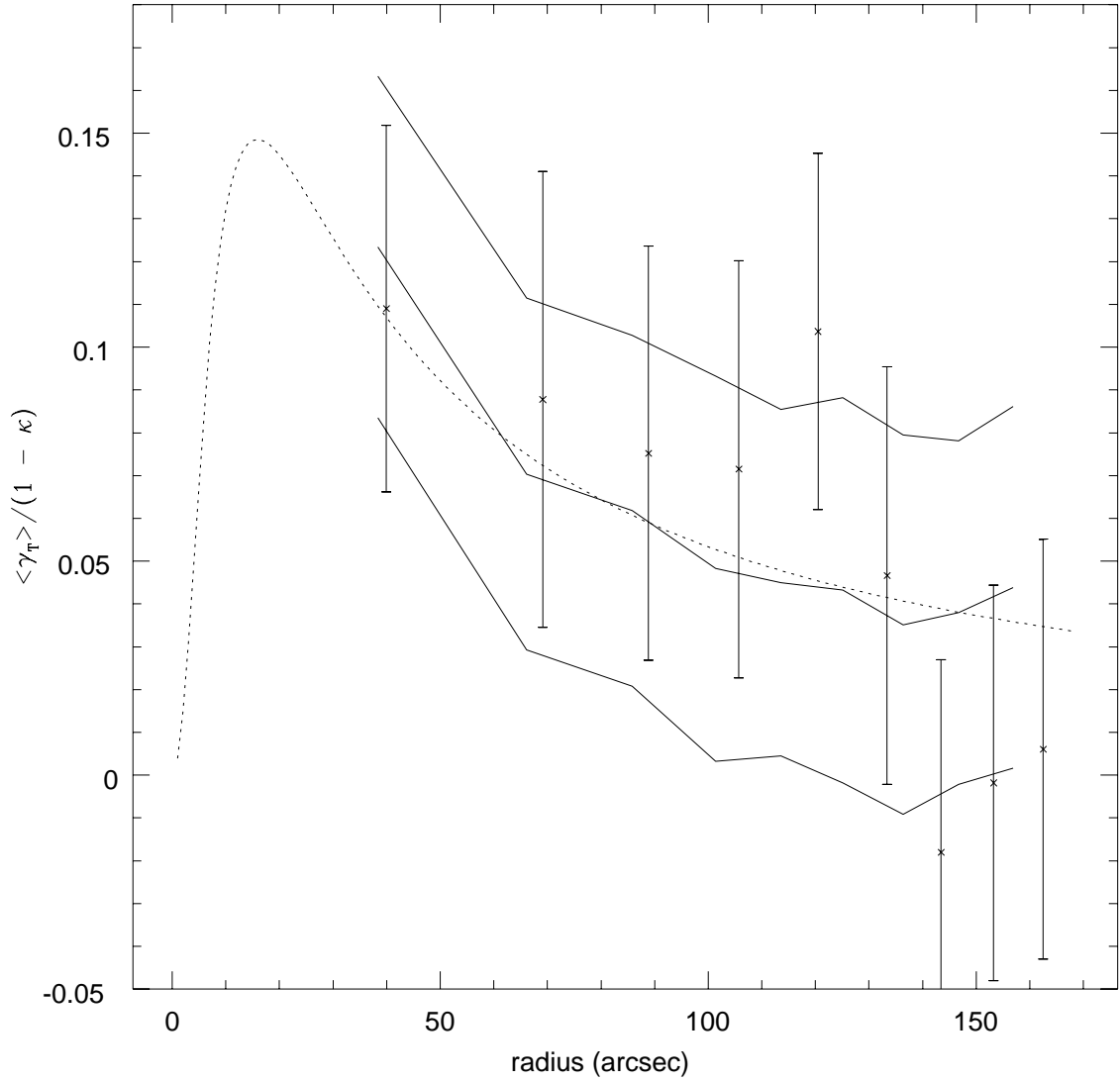


Fig. 12.— A plot of tangential shear vs projected radius in radial bins containing 145 galaxies each ($10'' \leq r \leq 168''$, $24.0 \leq V \leq 26.5$), centered on G1. The points are from the data and the solid lines are the mean and 1σ upper and lower error bands from 153 Monte-Carlo simulations. The dashed line is the input model for the simulations (Eqn. 8) and has $r_c = 10''$ and $\Sigma_0 = 0.615\Sigma_{crit}$. The dashed line is *not* averaged over the bins